

COMBINED EVALUATION OF BUBBLE DYNAMICS, POLYDISPERSION MODEL AND TURBULENCE MODELING FOR ADIABATIC TWO-PHASE FLOW

S. Mimouni, C. Baudry, M. Guingo, M. Hassanaly, J. Lavieville, N. Mechitoua, N. Méricoux.

Electricité de France, R&D Division
6 Quai Watier, 78401 Chatou, France
Stephane.mimouni@edf.fr

ABSTRACT

The paper deals with the modelling and the numerical simulation of upward bubbly flow in a new experimental test, named CHAPTAL. The CHAPTAL experimental program has been set up in the framework of the NEPTUNE project. Its aim is to locally characterize the hydraulics (phase topology and dynamic quantities) of an adiabatic high pressure bubbly flow in a vertical tube.

The CHAPTAL test section is a 5 m long vertical pipe with an inside diameter of 38 mm. The CHAPTAL test deals with pressure up to 10 bars. The working liquid fluid is water. Gas bubbles are made of R116 refrigerant fluid. The resulting flow is an adiabatic two-phase flow.

R116 wall injection creates bubbles of 2 to 4 mm outer diameter. The local measurements characterize each phase at three elevations with bi-hot-film and bi-optical probes.

Concerning the liquid phase, mean axial velocity, mean radial velocity, axial turbulent intensity and radial turbulent intensity are measured by the bi-hot-film probes. Concerning the gaseous phase, void fraction, interface velocity, interfacial area concentration and mean Sauter diameter are measured by bi-optical probes.

The paper aims at providing new measurements of an upward bubbly flow, for which non-dimensional numbers are representative of pressurized water reactor (PWR) conditions. Interfacial momentum transfer, polydispersion and turbulence modeling are evaluated in this context.

KEYWORDS

bubbly flow, CHAPTAL, turbulent intensity.

INTRODUCTION

The aim of the paper is to evaluate the combined effects of bubble dynamics and bubble size modeling for adiabatic two-phase flows. The main phenomena are the bubble coalescence, the bubble break-up and the forces acting on bubbles. Their modeling depends on turbulent quantities and uses some empirical relations. Conclusions drawn from agreement between experiments and computations could be biased because of discrepancies on turbulent variables. Thus, first we have to select a turbulence modeling related to the industrial prospects envisaged. This topic is discussed on below.

In a Pressurized Water nuclear Reactor, an optimum heat removal from the surface of the nuclear fuel elements is very important for thermal margins and safety. This optimum can be reached by means of mixing blades. Thus, it is important that the turbulence modeling deal with rotation effects. As a consequence, a Reynolds Stress model (RSM) is used in the calculations.

For test conditions with a higher outlet quality, the condensation rate is lower and the bubble coalescence is more likely to occur. Thus, the bubble size increases and the assumption of spherical bubble becomes questionable. As a consequence, the forces acting on bubbles are modified. In particular [16-17], due to bubble deformation, the lift force can change sign and moves the large bubbles (above a critical size) towards the pipe axis and move the small bubbles towards the wall. Then the void fraction profile is modified and has a peak at the pipe axis. Moreover, the bubble deformation decreases when the surface tension increases. This effect is taken into account by an effect of the Eotvos number in the lift force coefficient. Thus, the forces exerted on bubbles depend on this non dimensional number.

Another important feature for upward boiling bubbly flow is the simultaneous existence of several bubble sizes. It results in a relative velocity between bubbles of different sizes which enhances the bubbles collisions and then the coalescence.

In all cases, the modeling of forces exerted on bubbles is crucial to predict accurately all the computed variables. However, the coupling between condensation, coalescence, break-up, relative velocity, forces exerted on bubbles, and turbulence makes the modeling task difficult. Thus, the paper deals with the modelling and the numerical simulation of upward bubbly flows without phase change with a new experimental test, named CHAPTAL.

Besides, detailed information on the motion of gas bubbles in a liquid, both experimental and theoretical, is available in the literature [1-7-8-10-15-16-17]. Most of them are related to the motion of air bubbles in water and only a few works have been focused on different fluids. One objective of the experimental program is to provide experimental data for a range of non-dimensional numbers relatively unexplored.

This paper is organized as follows. First, the general model used for bubbly flow simulations is presented in section 2. The CHAPTAL experiment is briefly described in section 3. Then the comparison of the NEPTUNE_CFD calculation results and the experimental data is presented. Finally, conclusions are drawn about our current capabilities to simulate bubbly flow and perspectives for future work are given.

1. THE NEPTUNE_CFD SOLVER AND PHYSICAL MODELLING

1.1 Introduction

NEPTUNE_CFD is a three dimensional two-fluid code developed more especially for nuclear reactor applications. This local three-dimensional module is based on the classical two-fluid one pressure approach, including mass, momentum and energy balances for each phase.

The NEPTUNE_CFD solver, based on a pressure correction approach, is able to simulate multi-component multiphase flows by solving a set of three balance equations for each field (fluid component and/or phase) [4-13-14]. These fields can represent many kinds of multiphase flows: distinct physical components (e.g. gas, liquid and solid particles); thermodynamic phases of the same component (e.g.: liquid water and its vapour); distinct physical components, some of which split into different groups (e.g.: water and several groups of different diameter bubbles); different forms of the same physical components (e.g.: a continuous liquid field, a dispersed liquid field, a continuous vapour field, a dispersed vapour field). The solver is based on a finite volume discretisation, together with a collocated arrangement for all variables. The data structure is totally face-based, which allows the use of arbitrary shaped cells (tetraedra, hexahedra, prisms, pyramids ...) including non conforming meshes (meshes with hanging nodes)[21]. NEPTUNE_CFD inherits the I/O and HPC capabilities of the EDF open-source CFD software *Code_Saturne* [22], and can be used as a module of the SALOME plate-form.

1.2 Governing equations and physical modelling

The CFD module of the NEPTUNE software platform is based on the two-fluid approach [6-3]. In this approach, a set of local balance equations for mass, momentum and energy is written for each phase.

These balance equations are obtained by ensemble averaging of the local instantaneous balance equations written for the two phases. When the averaging operation is performed, the major part of the information about the interfacial configuration and the microphysics governing the different types of exchanges is lost. As a consequence, a number of closure relations (also called constitutive relations) must be supplied for the total number of equations (the balance equations and the closure relations) to be equal to the number of unknown fields. We can distinguish three different types of closure relations: those which express the inter-phase exchanges (interfacial transfer terms), those which express the intra-phase exchanges (molecular and turbulent transfer terms) and those which express the interactions between each phase and the walls (wall transfer terms). The balance equations of the two-fluid model we use for two-phase boiling flows and their closure relations are described in the following subsections.

1.2.1 Main set of balance equations

The two-fluid model we use for our two-phase boiling flow computations consists of the following balance equations.

Two mass balance equations:

$$\frac{\partial \alpha_k \rho_k}{\partial t} + \nabla \cdot (\alpha_k \rho_k \underline{V}_k) = \Gamma_k \quad k = l, g \quad (1)$$

where t is the time, α_k , ρ_k , \underline{V}_k denote the time fraction of phase k , its averaged density and velocity. The phase index k takes the values l for the liquid phase and g for gas bubbles.

Two momentum balance equations:

$$\frac{\partial \alpha_k \rho_k \underline{V}_k}{\partial t} + \nabla \cdot (\alpha_k \rho_k \underline{V}_k \underline{V}_k) = -\alpha_k \nabla p + \underline{M}_k + \alpha_k \rho_k \underline{g} + \nabla \cdot [\alpha_k (\underline{\Sigma}_k + \underline{R}_k)] \quad k = l, g \quad (2)$$

where p is the pressure, \underline{g} is the gravity acceleration, \underline{M}_k is the interfacial momentum transfer per unit volume and unit time, and $\underline{\Sigma}_k$ and \underline{R}_k denote the molecular and turbulent stress tensors, the latter being also called the Reynolds stress tensor. The wall friction terms for the two phases do not appear in the momentum balance equations because solid walls are only present at the boundaries of the flow domain and the wall friction is expressed through the wall boundary conditions.

1.2.2 interfacial transfer of momentum

The interfacial transfer of momentum \underline{M}_k appearing in the RHS of Eq. (2) is assumed to be the sum of five forces:

$$\underline{M}_k = \underline{M}_k^D + \underline{M}_k^{AM} + \underline{M}_k^L + \underline{M}_k^{TD} + \underline{M}_k^W \quad (3)$$

The five terms are the averaged drag, added mass, lift, turbulent dispersion and wall force forces per unit volume. Now we will give the expressions we use for these forces and for their coefficients.

Drag force:

$$\underline{M}_g^D = -\underline{M}_l^D = -\frac{1}{8} A_i \rho_l C_D |\underline{V}_g - \underline{V}_l| (\underline{V}_g - \underline{V}_l) \quad (4)$$

where C_D is the drag coefficient for bubbles and can be determined experimentally. It has been empirically modelled by Ishii [7]:

$$C_D = \frac{2}{3}d\sqrt{\frac{g|\rho_g - \rho_l|}{\sigma}}\left(\frac{1+17.67(f(\alpha))^{6/7}}{18.67f(\alpha)}\right) \quad \text{with} \quad f(\alpha) = (1-\alpha)^{1.5} \quad \text{for distorted bubbles} \quad (5)$$

$$C_D = \frac{8}{3}(1-\alpha)^2 \quad \text{for churn - turbulent regime}$$

Added-mass force:

$$\underline{M}_g^{AM} = -\underline{M}_l^{AM} = -C_A^{lg} \frac{1+2\alpha_g}{1-\alpha_g} \alpha_g \rho_l \left[\left(\frac{\partial \underline{V}_g}{\partial t} + \underline{V}_g \cdot \underline{\nabla} \underline{V}_g \right) - \left(\frac{\partial \underline{V}_l}{\partial t} + \underline{V}_l \cdot \underline{\nabla} \underline{V}_l \right) \right] \quad (6)$$

where C_A^{lg} is the added mass coefficient which is equal to $\frac{1}{2}$ for a spherical bubble and the factor $(1+2\alpha)/(1-\alpha)$ takes into account the effect of the bubbles concentration [20].

Lift force:

$$\underline{M}_g^L = -\underline{M}_l^L = -C_L \alpha_v \rho_l (\underline{V}_g - \underline{V}_l) \wedge (\underline{\nabla} \wedge \underline{V}_l) \quad (7)$$

where C_L is the lift coefficient. This coefficient is equal to $\frac{1}{2}$ in the particular case of a weakly rotational flow around a spherical bubble in the limit of infinite Reynolds number [2]. It has been empirically modelled by Tomiyama [17]:

If $Eo_H < 4$:

$$C_L = \min\{0.288 \tanh(0.121 \text{Re}), 0.00105 Eo_H^3 - 0.0159 Eo_H^2 - 0.0204 Eo_H + 0.474\} \quad (8)$$

If $4 \leq Eo_H \leq 10$:

$$C_L = 0.00105 Eo_H^3 - 0.0159 Eo_H^2 - 0.0204 Eo_H + 0.474 \quad (9)$$

If $Eo_H > 10$:

$$C_L = -0.27 \quad (10)$$

With the modified Eotvos number defined by:

$$Eo_H = \frac{g(\rho_g - \rho_l)d_H^2}{\sigma}$$

where d_H is the maximum horizontal dimension of the deformed bubble, which is calculated using an empirical correlation given by Wellek [19] :

$$d_H = D_b \sqrt[3]{1 + 0.163 Eo^{0.757}} \quad (11)$$

where D_b is the spherical equivalent bubble diameter and Eo has a similar expression as Eq. (12) with d instead of d_H .

Turbulent dispersion force:

$$\underline{M}_g^{TD} = -\underline{M}_l^{TD} = -C^{TD} \rho_l k_l \nabla \alpha_g, \quad (12)$$

Where C^{TD} is modelled as a function of drag coefficient, virtual mass coefficient and liquid and gas turbulent quantities [11].

The wall force is the one derived by Tomiyama et al. [16-17].

1.2.3 Turbulence modelling

In the field of fuel assembly analysis or design by means of CFD codes, the overwhelming majority of the studies are carried out using two-equation Eddy Viscosity Models (EVM) as turbulence model, especially the standard $K - \varepsilon$ model, while the use of Reynolds Stress Transport Models (RSTM) remains limited. In contrast, extensive testing and application over the past three decades have revealed a number of shortcomings and deficiencies in Eddy Viscosity Models. Indeed, the $K - \varepsilon$ model is totally blind to flow rotation, e.g. in the presence of swirls. This aspect is crucial for the simulation of a hot channel in a fuel assembly which is the main application of the CFD tool [13-14]. As a consequence, the liquid turbulence is modelled by the SSG-Rij-epsilon model [5].

In the K-equation, the turbulent reverse coupling is due to the turbulent production in the wakes and is roughly expressed as the work of the drag force. In order to generalize to SSG-Rij-epsilon approach, this term is distributed at the right hand side of the R11, R22 and R33 equations.

1.2.4 Bubble size modelling

The modeling of polydispersion in size has been developed for bubbly flow based on the moment density method [15].

The Eulerian evolution of the local instantaneous bubble population is described by the evolution of its size distribution function: f . The bubble number density, n (m^{-3}), is introduced as well as the probability density function P (m^{-1}) for a bubble of size D to be located at x at a given time t .

$$f(D, \vec{x}, t) = n(\vec{x}, t) P(D, \vec{x}, t) \quad (13)$$

With:

$$f = \begin{cases} \frac{3 n(\vec{x}, t) D}{4 D_1^3(\vec{x}, t)} (2D_1(\vec{x}, t) - D) & \text{if } D \leq 2D_1 \\ 0 & \text{otherwise} \end{cases} \quad (14)$$

D_1 being the mean diameter defined as the moment of order 1 over the moment of order 0.

f has been chosen as a quadratic law (eq. (14)) that has the two advantages of dealing with a spread in possible bubble sizes around its mean value and of possible analytical evaluation of integral source terms for the various moment density transport equations. Moreover, the quadratic shape of f has been validated against experimental data obtained on the boiling bubbly flow DEBORA facility [12-14].

This distribution function can be characterized by only two of its statistical moments, whose evolutions are solved throughout the flow thanks to transport equations. The two chosen moments are the moments of order 2 and 3 because they are related to essential two-phase flow variables namely the volumetric interfacial area a_i and the volumetric fraction of the dispersed phase.

We assume, for the bubbles, a mono-dispersion in velocity and temperature (e.g. locally, all the bubbles have the same velocity and the same temperature despite possible different diameters).

To obtain the closure terms, we evaluate the contribution of the various source terms related to the different phenomena involved: coalescence, break-up, nucleation, dilatibility/compressibility, phase change (modeling details are given in reference [15]). This modeling has been successfully validated on some TOPFLOW with obstacle tests and DEBORA tests [15]. Simulation results have been compared to local data such as bubble diameters, interfacial area, void fraction or liquid temperature distributions.

As a consequence, this bubble size modelling is used in all the calculations.

2. CHAPTAL EXPERIMENTAL PROGRAM: LOCAL MEASUREMENTS IN ADIABATIC TWO-PHASE FLOWS (WATER-R116 GAS)

The CHAPTAL experimental program has been set up in the framework of the NEPTUNE project [18]. Its aim is to locally characterize the hydraulics (phase topology and dynamic quantities) of an adiabatic high pressure bubbly flow in a vertical tube.

The CHAPTAL test section is a 5 m long vertical pipe with an inside diameter of 38 mm. The CHAPTAL test deals with pressure up to 10 bar. The working liquid fluid is water. Gas bubbles are made of R116 refrigerant fluid. The resulting flow is an adiabatic two-phase flow (Figure 1). R116 wall injection creates bubbles of 2 to 4 mm outer diameter.

The local measurements characterize each phase along diameters at different elevations with bi-hot-film and bi-optical probes. Local measurements are performed at three elevations: 15.3D, 52.1D and 115.3D, where D is the pipe diameter and is equal to 38 mm. Concerning the liquid phase, 35 hot film points have been measured along a diameter at each of the 3 elevations. A signal post-processing after elimination of passing through bubble signal contribution is used. Concerning gas phase, 19 optical probe measurement points along a radius at 3 test section elevations have been performed. Bubbles velocities are calculated by an ‘inter-correlation’ method.

Concerning the gaseous phase, void fraction, interface velocity, interfacial area concentration and mean Sauter diameter are measured by bi-optical probes.

During the second test series (2012), 10 thermal-hydraulic conditions have been investigated around the main condition (selected in order to consider only the bubbly flow regime) :

$$Q_l = 2,272\text{kg}\cdot\text{s}^{-1} \text{ +/-}20\% \text{ and } Q_g = 28\text{g}\cdot\text{s}^{-1} \text{ +/-}50\%.$$

The measurement uncertainties are given in the table on below:

Table I Measurement uncertainties	
Void fraction	± 0.01
Bubble velocity	± 10%
Interfacial area	± 10%
Sauter diameter	± 10%
Axial liquid velocity	± 7%

The non dimensional numbers range corresponding to the targeted PWR applications is described in table II. In order to represent phenomena as similar as possible to industrial applications but in conditions

allowing visualization and intrusive measurements, a simulant fluid is used in experiment (water – gas R116).

Table II : non dimensional numbers calculated in industrial applications							
	Re (x10 ⁵)	Fr	Re _d	Mo (x10 ⁻¹³)	Eo (x10 ⁻³)	We	$\frac{\rho_L}{\rho_G}$
Minimum	1.11	3	269	0.3	0.24	0.13	5.4
Maximum	10.9	40	8700	5.2	162	3.62	16.5

The dimensionless numbers are defined below:

- Reynolds number: $Re = \frac{V_m D}{\nu_m}$ with $V_m = \alpha_L V_L + \alpha_G V_G$, and D is the hydraulic diameter ;
- Bubble Reynolds number : $Re_d = \frac{V_r D_b}{\nu_L}$ with D_b the bubble diameter and V_r the relative velocity ;
- Morton number: $Mo = \frac{g \mu_L^4 \Delta \rho}{\rho_L^2 \sigma^3}$;
- Eötvös number : $Eo = \frac{g \Delta \rho D_b^2}{\sigma}$;
- Weber number: $We = (Re_d)^2 * \left(\frac{Mo}{Eo}\right)^{0.5} = \frac{\rho_L V_r^2 D_b}{\sigma}$;
- Froude number: $Fr = \frac{G}{\rho_m \sqrt{gD}}$;
- Jacob number : $Ja = \frac{\rho_L C_{p,L}}{\rho_G L} \Delta T$ where ΔT is the subcooled temperature ;
- Prandtl number : $Pr = \frac{\nu_L}{k_L}$.

3. NUMERICAL SIMULATION OF THE CHAPTAL EXPERIMENT

3.1 Boundary and initial conditions for computations

The set of physical properties is the following: $\rho_{gas} = 61.4 \text{ kg.m}^{-3}$, $\rho_{liquid} = 992.7 \text{ kg.m}^{-3}$,
 $P_0 = 9 \text{ bar}$, $g = 9.81 \text{ m.s}^{-2}$

Liquid and gas mass flow rate are imposed at inlet and are given in table III.

Table III : Thermal-hydraulics conditions

test	Liquid flow rate (kg/s)	Gas flow rate (g/s)
QI-2271-Qg-28	2.272	28.13
QI-2271-Qg-42	2.267	42.08
QI-2271-Qg-14	2.271	14.18
QI-2725-Qg-28	2.725	28.02
QI-1817-Qg-28	1.816	28.13
QI-1136-Qg-14	1.132	14.16

3.2 Computational strategy and convergence results

The flow is assumed to be axi-symmetric therefore a two-dimensional axi-symmetric meshing is used. A first set of computations have been performed on four kinds of meshing for the case QI-2271-Qg-42 : a very coarse grid (10 cells in the radial direction and 250 cells in the axial direction), a coarse grid (20 cells in the radial direction and 500 cells in the axial direction), a medium grid (40 cells in the radial direction and 1000 cells in the axial direction) and a fine grid (80 cells in the radial direction and 2000 cells in the axial direction). Results are similar except for the very coarse mesh (Figure 2). As a consequence, the following computations are done using the medium grid.



Figure 1: Visualization of bubbles of R116

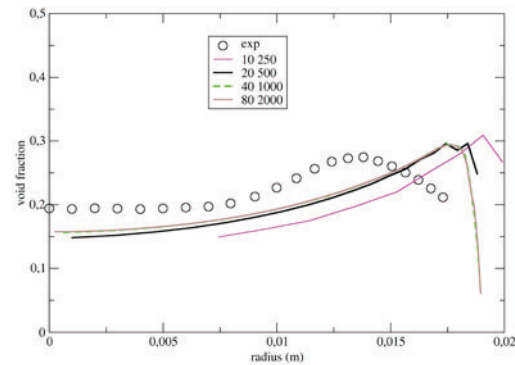


Figure 2: General sensitivity to the mesh refinement for the radial profile of void fraction

3.3 Numerical results and discussion

We compare numerical results against experimental data for the radial profiles of the axial liquid velocity, the axial gas velocity, the void fraction, the interfacial area and the axial (zz) and radial (xx) Reynolds stress components.

These quantities are measured at three elevations: 15.3D, 52.1 D and 115.3 D. Corresponding curves are respectively red, blue and green. Numerical values are represented par dotted lines whereas experimental values are represented by squared symbols.

Bubble diameter and Reynolds stress components:

The cases QI-1136-Qg-14 and QI-1817-Qg-28 are characterized by a small value of the liquid mass flow rate at inlet. In both cases, bubbles diameter increase with height (Figure 3-Figure 9): the coalescence phenomenon is dominant over the break-up phenomenon. In computations, the bubble diameter is

overestimated in the case QI-1136-Qg-14 (Figure 7 - Figure 8) but in a reasonable agreement in the case QI-1817-Qg-28 (Figure 13 - Figure 14). Indeed, in the case QI-1817-Qg-28, the liquid turbulent kinetic energy is overestimated but in a reasonable agreement in the case QI-1136-Qg-14 which means that break-up is overestimated in the case QI-1817-Qg-28.

As a consequence, the ratio coalescence/break-up is slightly overestimated in the modelling.

It is worth noting that the liquid turbulent kinetic energy increases with height (cases QI-1136-Qg-14 and QI-1817-Qg-28) which is correctly reproduced by the CFD tool. The situation is actually different in others cases where the liquid mass flow rate at inlet is about two times greater (Figure 19-Figure 24-Figure 25-Figure 30-Figure 36-Figure 37). Indeed, in QI-2271-Qg-14 test and QI-2775-Qg-25 test, the liquid turbulent kinetic energy decreases with height (Figure 19-Figure 36-Figure 37). This tendency is correctly predicted which is very encouraging. From the bottom to the middle level, this high value of turbulent intensity enhances break-up when bubbles migrate towards regions of low bubbles density : as a consequence, the bubbles diameter decrease below the initial value at inlet (Figure 16-Figure 32).

Unfortunately, even if computations are quantitatively in reasonable agreement with experimental data for the bubble diameter, this particular effect is not correctly taken into account by the polydispersion model. But, the accuracy of the turbulence modeling could help to improve the break-up and coalescence modeling in further computations.

Anyway, the measurements of the turbulent stress components provided by CHAPTAL tests are of relevant interest to improve the prediction of the bubbles diameter.

Axial velocity

Computations and experimental values of water axial velocities and R116 axial velocities are in a good agreement (Figure 5-Figure 6-Figure 11-Figure 12-Figure 17-Figure 18-Figure 22-Figure 23-Figure 28-Figure 29-Figure 34-Figure 35).

Void fraction

It is well-known that for low values of E_o (small bubble diameter) bubbles migrate toward the wall whereas for large values of E_o , bubbles migrate towards the axis pipe flow. This behaviour is reproduced for all cases (Figure 4-Figure 10-Figure 16-Figure 21-Figure 27-Figure 33). As a consequence, it is crucial to calculate accurately the bubble diameter for predicting the void fraction. A reasonable agreement is obtained between calculated and experimental values for the void fraction. It is worth noting that a good agreement is obtained for two cases (QI-2271-Qg-14 - QI-2775-Qg-25) (Figure 16-Figure 33). These two cases correspond to the highest values of the ratio liquid mass flow rate / gas mass flow rate. The characteristic time of bubble-bubble interaction is the lowest for these two cases.

4. CONCLUSIONS AND PERSPECTIVE

In the framework of the nuclear industry, a CFD tool has been developed and advanced models dedicated to boiling flows have been implemented and validated against experimental data. In order to improve the models, experimental programs as CHAPTAL program have been launched to investigate separated effects like bubble dynamics without phase change. The aim of the paper was to evaluate the combined effects of bubble dynamics and bubble size modeling for adiabatic two-phase flows. The main phenomena are the bubble coalescence, the bubble break-up and the forces acting on bubbles and their modeling depends on turbulent quantities. In this context, fluctuating velocities have been measured at three levels in a pipe: at the bottom, middle and at the top. Measurements of liquid and gas velocities, void fraction, bubble diameter and void fraction provide crucial details to understand the main physical phenomena and to model them.

7. M. Ishii; Two-fluid model for two-phase flow, *Multiphase Science and Technology*, Hewitt G.F., Delhaye J.M., Zuber N. Eds., Vol. **5**, pp. 1-58 (1990).
8. A.M. Kamp, A.K. Chester, C. Colin, J. Fabre, “bubble coalescence in turbulent flows: a mechanistic model for turbulence induced coalescence applied to microgravity bubbly pipe flow”, *Int. J. Heat Mass Transfer* **38** (2001) 481-493.
9. Eckhard Krepper, Dirk Lucas, Thomas Frank, Horst-Michael Prasser, Phil J. Zwart, “The inhomogeneous MUSIG model for the simulation of polydispersed flows”, *Nuclear Engineering and Design*, Volume **238**, Issue 7, July 2008, Pages 1690-1702.
10. E. Krepper, B. Koncar, Y. Egorov, “CFD modelling of subcooled boiling – Concept, validation and application to fuel assembly design”, *Nuclear Engineering and Design* **237** 716-731 (2007).
11. J. Lavieville et al, “A Generalized Turbulent Dispersion Model for bubbly flow numerical simulation in NETPUNE_CFD”, *The 16th International Topical Meeting on Nuclear Reactor Thermal Hydraulics (NURETH-16)*, Chicago, IL, USA, August 30-September 4, 2015
12. E. Manon, "Contribution à l'analyse et à la modélisation locale des écoulements bouillants sous-saturés dans les conditions des Réacteurs à Eau sous Pression", PhD thesis, Ecole Centrale Paris, 2000.
13. S. Mimouni, F. Archambeau, M. Boucker, J. Laviéville, and C. Morel, A second order turbulence model based on a Reynolds Stress approach for two-phase flow – Part I: adiabatic CASES, *Sciences and Technology of Nuclear Installations*, Volume **2009** (2009), Article ID 792395, 14 pages.
14. S. Mimouni, F. Archambeau, M. Boucker, J. Laviéville, C. Morel, “A second order turbulence model based on a Reynolds Stress approach for two-phase boiling flow and application to fuel assembly analysis”, *Nuclear Engineering and Design*, Volume **240**, Issue 9, September 2010, Pages 2225-2232.
15. P. Ruyer, N. Seiler, M. Beyer, F.P. Weiss, "A bubble size distribution model for the numerical simulation of bubbly flows", *6th International Conference on Multiphase Flow, ICMF* . Leipzig, Germany, July 9-13 (2007).
16. A. Tomiyama, A., “Struggle with computational bubble dynamics”, *3rd Int. Conf. Multiphase Flow ICMF'98*, Lyon, France, June 8-12 (1998).
17. A. Tomiyama, K. Sakoda, G.P. Celata, I. Zun, “A simple method for evaluating fluctuating bubble velocity and its application to a hybrid bubble tracking method”, *3rd Int. Symposium on Two-Phase Flow Modelling and Experimentation*, Pisa, Italy, September 22-24 (2004).
18. P. Vasseur, “Projet NEPTUNE lot 3.3, Rapport d'essais de la campagne 2009 du programme expérimental CHAPTAL », H-I84-2009-01230-FR, Nept_2009_L3.3/03, technical report in french.
19. R.M Wellek, A.K Agrawal, A.H.P Skelland, “Shape of liquid drops moving in liquid media”, *AIChE J.*, **12** (1966), pp. 854–862
20. N. Zuber, “On the dispersed two-phase flow in the laminar flow regime”, *Chem. Eng. Sc.*, No. **19**, p. 897 (1964).
21. N. Méchitoua, M. Boucker., J. Laviéville, J.-M. Hérard, S. Pigny, G. Serre, “An unstructured finite volume solver for two-phase water/vapor flows modelling based on an elliptic-oriented fractional step method”, *Proceedings of NURETH-10*, Seoul, (5-9 October 2003).
22. N. Archambeau, N. Méchitoua, M. Sakiz., “Code *Saturne*: a finite volume code for the computation of turbulent incompressible flows- Industrial Applications”, *Int. J. on Finite Volumes*, <http://www.latp.univ-mrs.fr/IJFV/>, **Vol.1**, 2004.

case QI-1136-Qg-14 : Ql = 1.132 kg/s, Qg = 14.16 g/s

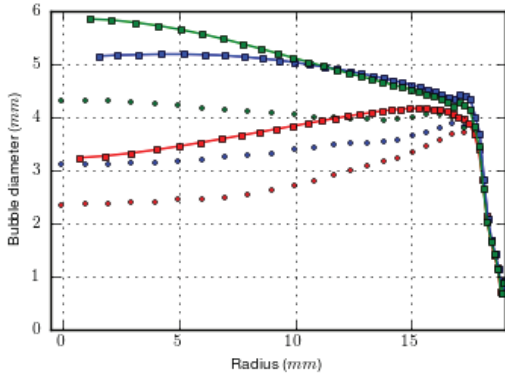


Figure 3: Bubble diameter

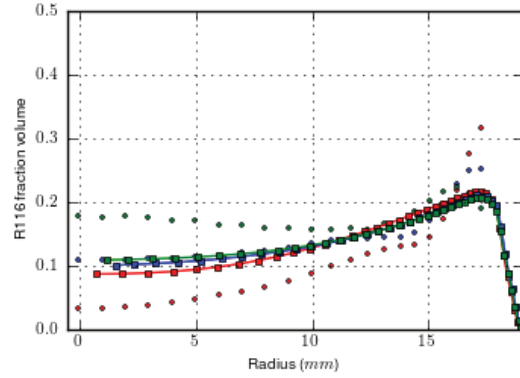


Figure 4: Void fraction

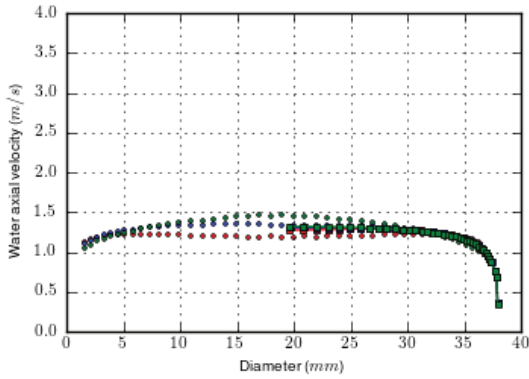


Figure 5: Water axial velocity

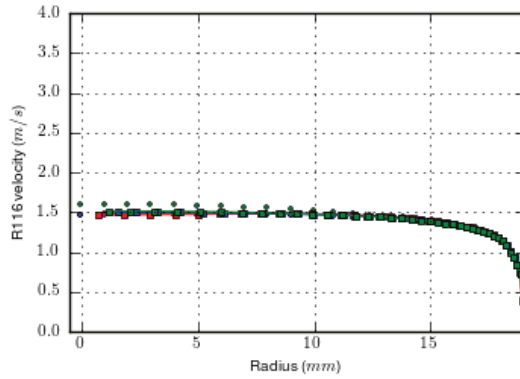


Figure 6: R116 axial velocity

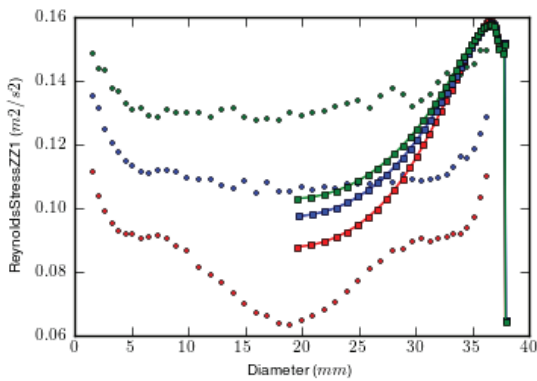


Figure 7: RZZ

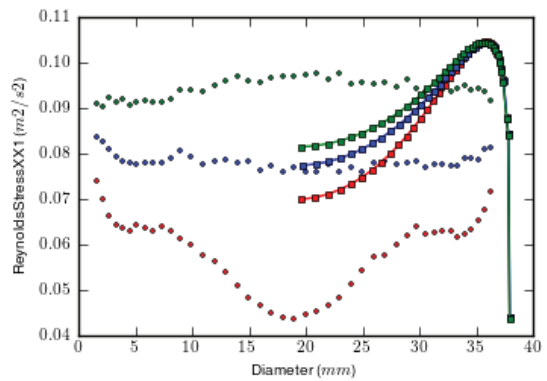


Figure 8: Rxx

case Q1-1817-Qg-28 : Ql = 1.816 kg/s, Qg = 28.13 g/s

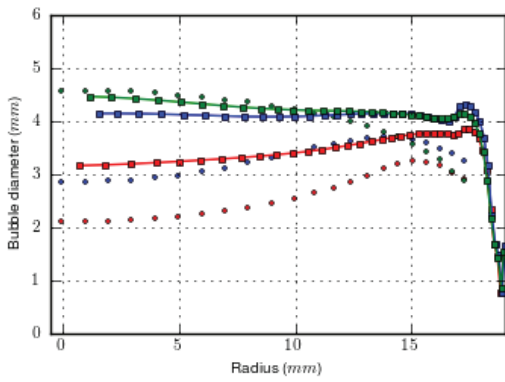


Figure 9: Bubble diameter

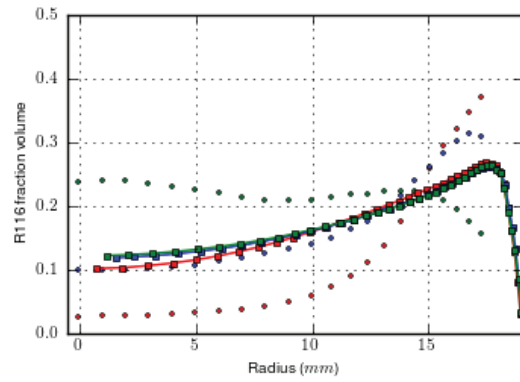


Figure 10: Void fraction

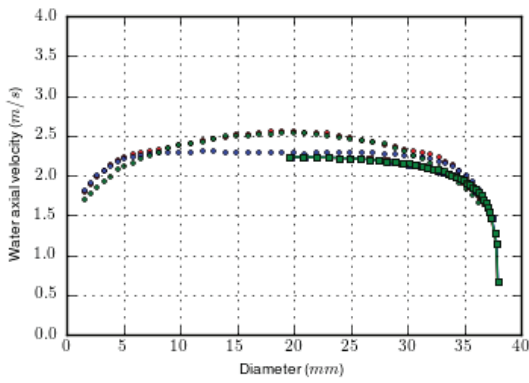


Figure 11: Water axial velocity

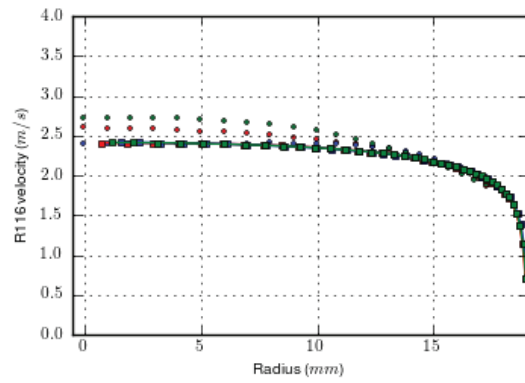


Figure 12: R116 axial velocity

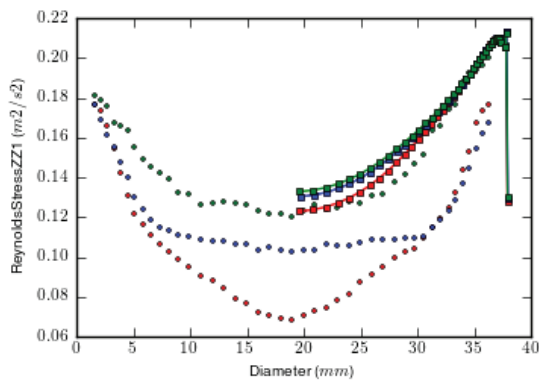


Figure 13: Rzz

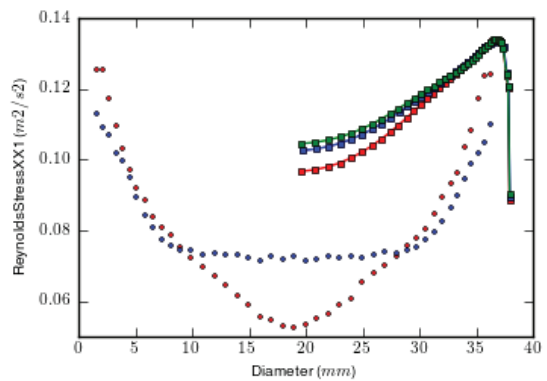


Figure 14: Rxx

case Q1-2271-Qg-14 : Ql = 2.271 kg/s, Qg = 14.18 g/s

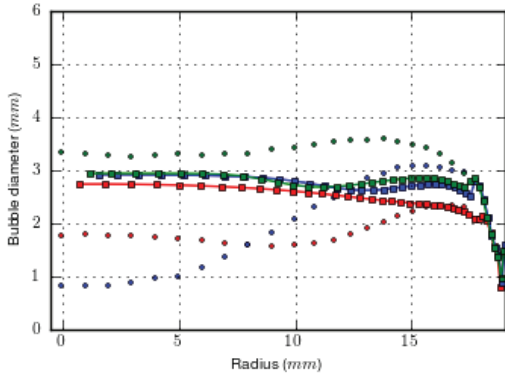


Figure 15: Bubble diameter

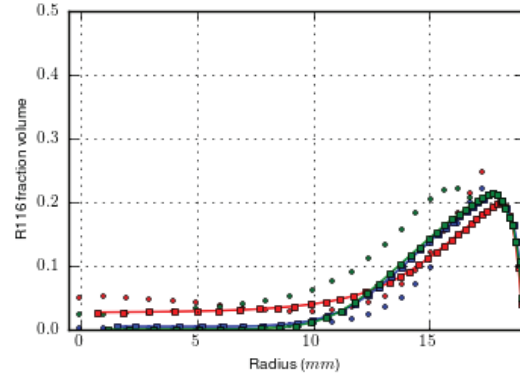


Figure 16: Void fraction

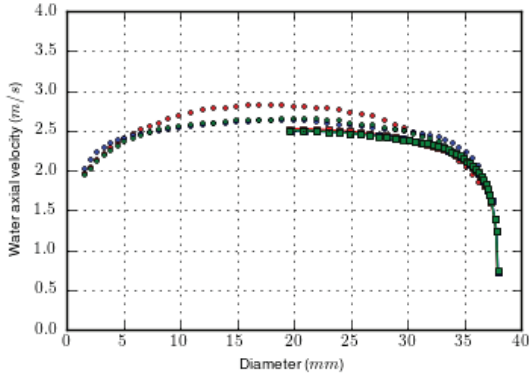


Figure 17: Water axial velocity

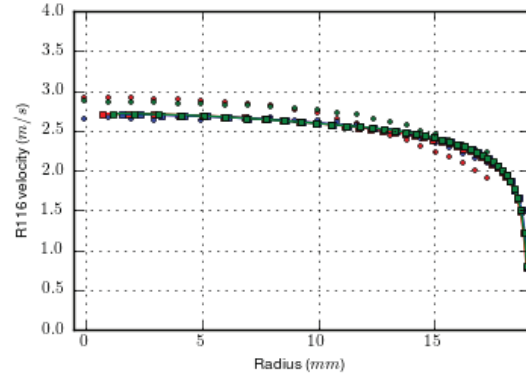


Figure 18: R116 axial velocity

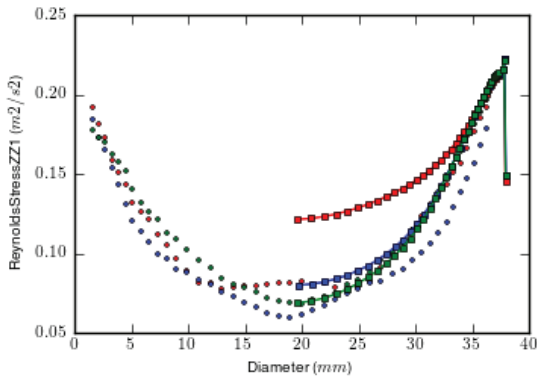


Figure 19: Rzz

case Q1-2271-Qg-28 : Ql = 2.272 kg/s, Qg = 28.13 g/s

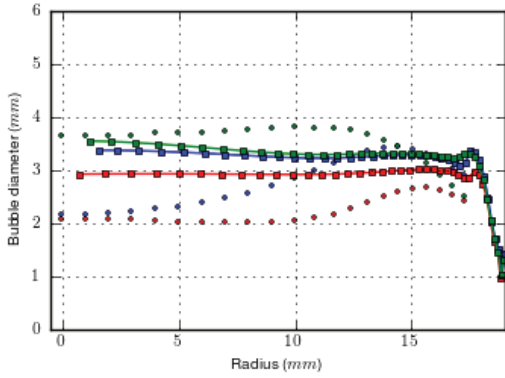


Figure 20: Bubble diameter

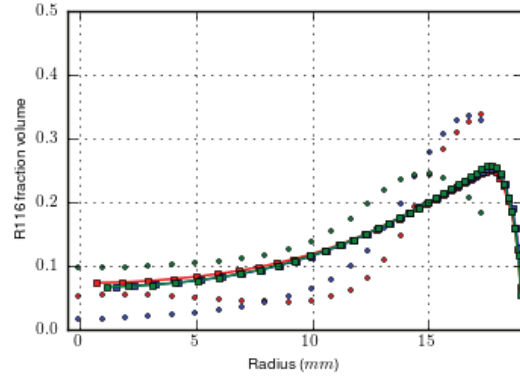


Figure 21: Void fraction

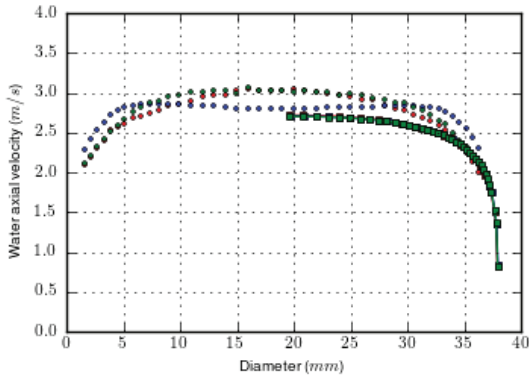


Figure 22: Water axial velocity

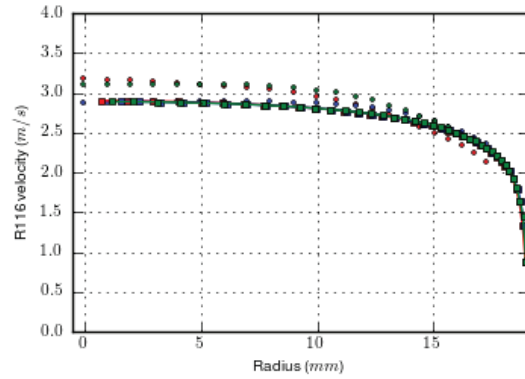


Figure 23: R116 axial velocity

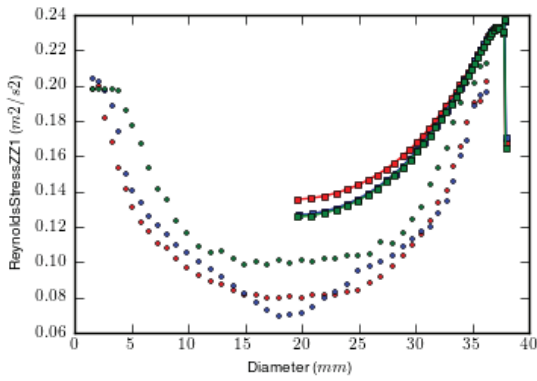


Figure 24: Rzz

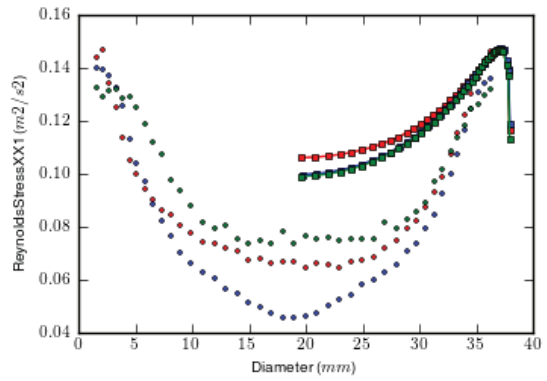


Figure 25: Rxx

case Q1-2271-Qg-42 : Ql = 2.267 kg/s, Qg = 42.08 g/s

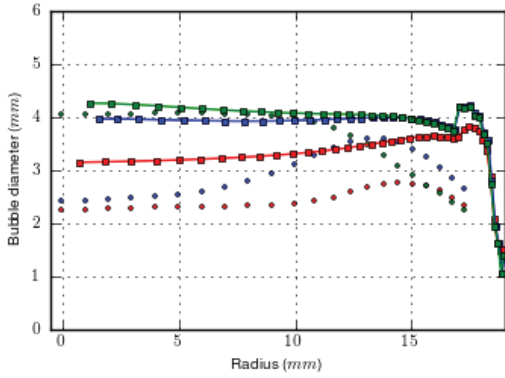


Figure 26: Bubble diameter

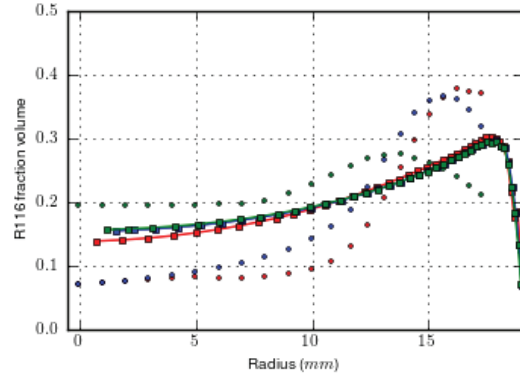


Figure 27: Void fraction

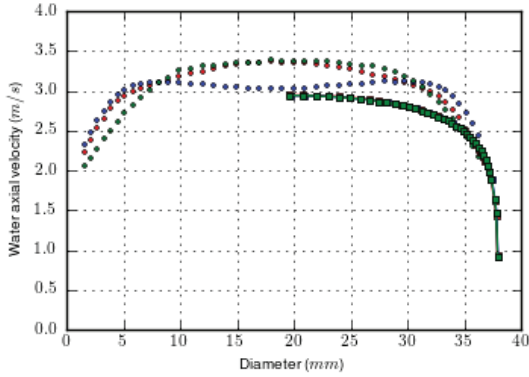


Figure 28: Water axial velocity

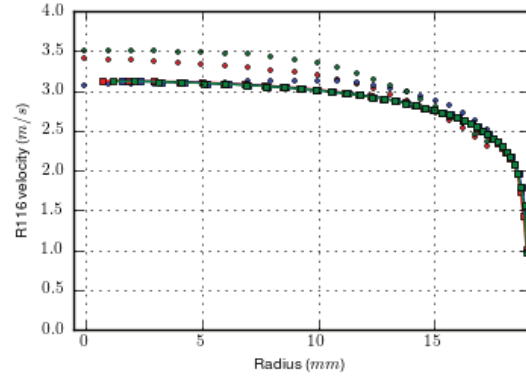


Figure 29: R116 axial velocity

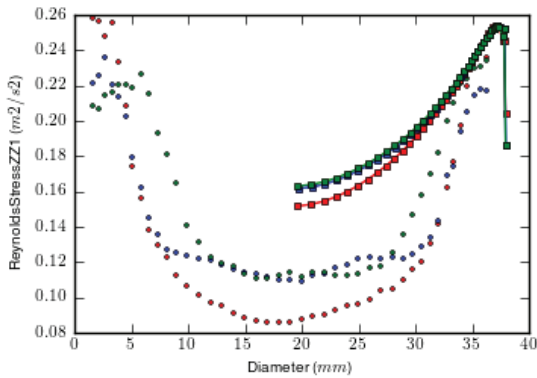


Figure 30: Rzz

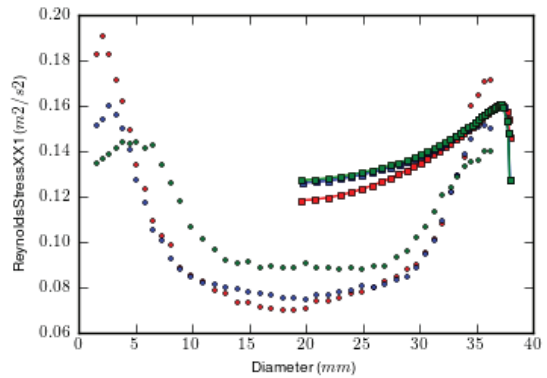


Figure 31: Rxx

case Q1-2775-Qg-28 : Ql = 2.725 kg/s, Qg = 28.02 g/s

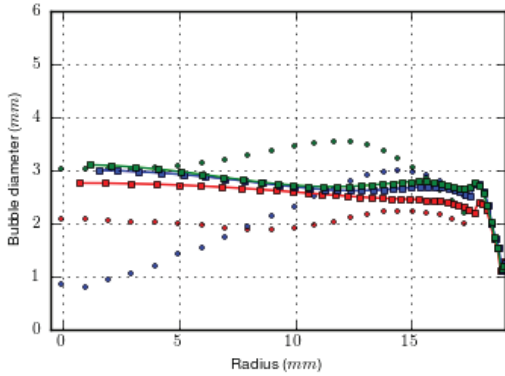


Figure 32: Bubble diameter

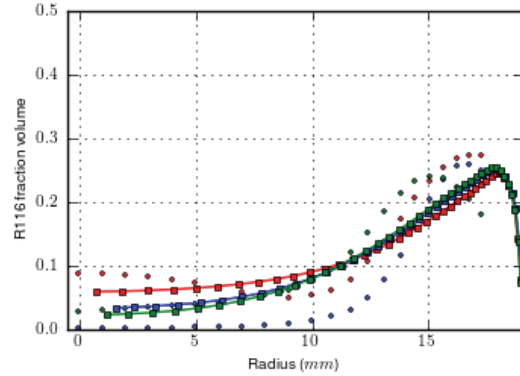


Figure 33: Void fraction

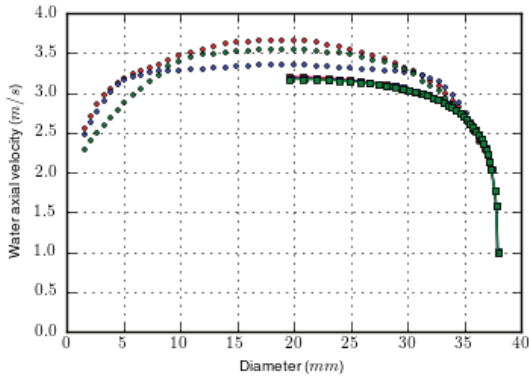


Figure 34: Water axial velocity

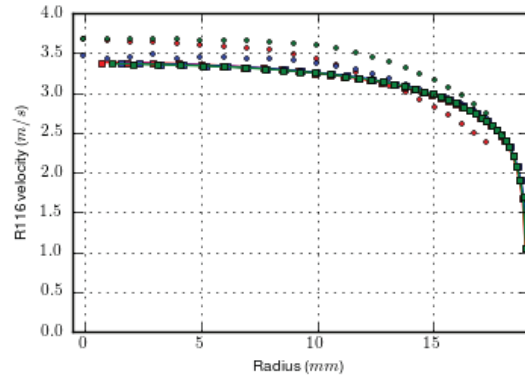


Figure 35: R116 axial velocity

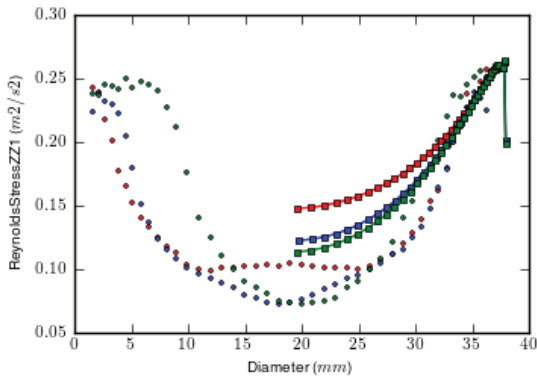


Figure 36: Rzz

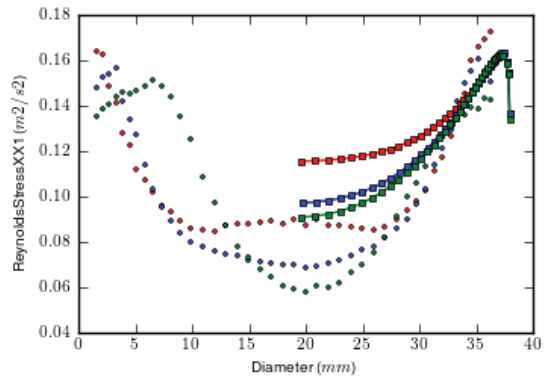


Figure 37: Rxx